

FREAK WAVE GENERATION IN A WAVE BASIN WITH HOSM-WG METHOD

Hidetaka Houtani

National Maritime Research Institute
Mitaka, Tokyo, Japan

Takuji Waseda

The University of Tokyo
Kashiwa, Chiba, Japan

Wataru Fujimoto

The University of Tokyo
Kashiwa, Chiba, Japan

Keiji Kiyomatsu

The University of Tokyo
Kashiwa, Chiba, Japan

Katsuji Tanizawa

National Maritime Research
Institute, Mitaka, Tokyo, Japan

ABSTRACT

A method to produce freak waves with arbitrary spectrum in a fully directional wave basin is presented here. This is an extension of Waseda, Houtani and Tanizawa at OMAE 2013[1], which used "HOSM-WG" based on the higher-order spectral method (HOSM). We used the following three methods to improve the HOSM-WG in [1]: "separation of free waves from bound waves," "using Biesel's transfer function in wavenumber space" and "using Schaffer's 2nd-order wave maker control method." Modulational wave trains, freak waves in unidirectional irregular waves and freak waves in short-crested irregular waves were generated in a wave basin. The experimental results using the improved HOSM-WG were compared to the HOSM simulation, and good agreements were found. The effectiveness of the improved HOSM-WG was ascertained. We showed that the difference between HOSM-WG and HOSM simulations became larger as wave steepness, frequency bandwidth of the spectrum or directional spreading became larger.

INTRODUCTION

Recent studies have revealed that the probability of freak wave occurrence increases as the frequency bandwidth of the spectrum narrows [2-5]. It has also been revealed that the probability of freak wave occurrence increases as the directional spreading of the spectrum narrows [6-9]. These results show that the modulational instability due to quasi-resonant interaction plays an important role in freak wave generation. Moreover, recent studies have suggested that the quasi-resonant interaction affects the local geometric and kinematic features of freak waves [10, 11].

A recent study has shown that a number of ship accidents near Japan occurred in freakish sea states when the frequency

bandwidth and the directional spreading of the spectrum narrowed [12]. However, it is impossible to know whether a ship had actually encountered a freak wave or not. Even if a ship had encountered a freak wave, its effects on the structure and motion of the ship is not evident. Therefore, it is of great importance to reproduce freak waves in an experimental wave basin, under the sea state at the time of the accident.

The methods to generate freak or large waves in an experimental wave basin based on linear wave theory have been developed. These methods can be classified as the phase speed method, the reverse dispersion method and the group celerity method ([13] and the references therein). Generated waves based on these methods behave quite differently from those based on the linear wave theory near the focal point due to strong nonlinearity. Some correction methods taking into account of the nonlinear effects have been developed, such as phase correction [13] or phase speed correction [14-16]. Some studies have extended these methods to the short-crested waves and have reproduced freak or large waves in an experimental wave basin taking into account of the directional spectrum of the actual sea [17, 18].

However, it is also important to take into account of quasi-resonant interaction for the freak waves generated in an experimental wave basin. The theory of (quasi-)resonant interaction has been developed in the form of the temporal evolution of the spatially periodic wave trains (cf. Zakharov 1967 [19]). For the case of unidirectional waves, the coordinate transformation switching space and time can easily be applied, so the spatial evolution of the temporally periodic wave trains due to modulational instability can be investigated in a tank experiment [20]. A large wave generation system based on the spatial evolution of modulational wave trains has been developed [21].

However, this coordinate transformation cannot directly be applied to directional waves because the space has two dimensions though time has only one dimension. To overcome this difficulty, a method named ‘‘HOSM-WG’’ to generate wave trains that are periodic in space and evolve in time according to (quasi)-resonant interaction has been proposed [1]. The wave maker signals for the HOSM-WG are calculated based on the simulation by the HOSM (Higher-Order Spectral Method; [22, 23]). The temporally evolving modulational wave trains that were simulated by the HOSM were well reproduced in a wave basin by the HOSM-WG in the study [1].

In an earlier study [24], experiments on unidirectional irregular wave generation were conducted, and the results were reproduced numerically by the HOSM; they showed a good agreement. A 3-dimensional numerical wave tank, called the HOST, based on HOSM was developed [25]. The experimental results of directional wave generation were compared with the corresponding simulation with the HOST, and a good agreement between them was shown. In these studies, the wave generation was based on the linear wave theory, which means that the generated waves evolved in space. The HOSM-WG is different from these studies in this regard.

In this study, we improve the HOSM-WG method to generate freak waves in unidirectional irregular waves and in short-crested irregular waves. We then show the results of experimental validation of the HOSM-WG.

WAVE GENERATION BASED ON HOSM

Experimental Facility

Wave generation experiments were conducted in the Actual Sea Model Basin (ASMB hereafter) and 2-dimensional Wave Tank (WT hereafter) at the National Maritime Research Institute of Japan. ASMB is 76.2 m by 36.0 m and 4.5 m deep and is fully surrounded by 382 flaps that enable us to generate directional waves in full spectral dimension (Fig. 1). All the flaps are equipped with capacitance wave gauges in front of them in order to absorb incident waves. Details of ASMB can be found in [17, 26]. WT is 50.0 m by 8.0 m and 4.5 m deep with a flap type wave maker. A beach is equipped at the opposite end of the tank (Fig. 2).

Conventional Wave Generation Theory

Wave maker theory was first derived by Havelock (1929) [27]. He derived the transfer function between wave maker motions and generated waves for the piston type wave maker. The validity of this theory was experimentally investigated [28]. The flap type wave maker theory was derived by Biesel and Suquet (1951) [29]. This transfer function is known as ‘‘Biesel’s transfer function.’’ Plunger type wave maker theory was also well established (cf. [30, 31]). These theories are all based on linear wave theory.

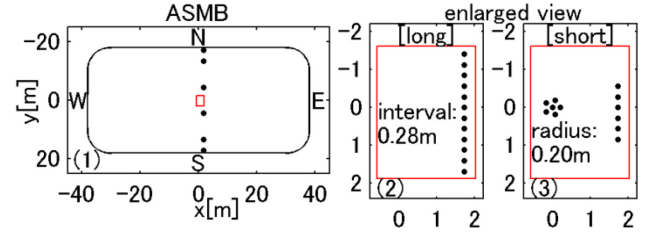


Figure 1. SCHEMATIC VIEW OF ACTUAL SEA MODEL BASIN (ASMB) AND WAVE GAUGE ARRANGEMENT: GENERAL VIEW (1), AND ENLARGED VIEW OF CENTER AREA FOR UNIDIRECTIONAL WAVE EXPERIMENTS (2) AND FOR SHORT-CRESTED WAVE EXPERIMENTS (3).

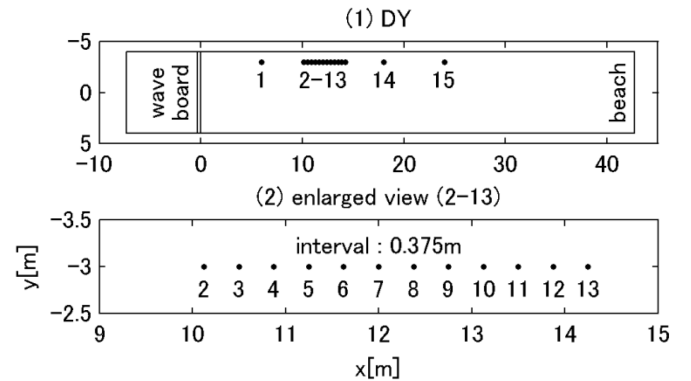


Figure 2. SCHEMATIC VIEW OF WAVE TANK (WT) AND WAVE GAUGE ARRANGEMENT IN WT: GENERAL VIEW (1) AND ENLARGED VIEW OF WAVE GAUGES #2- #13 (2).

It is known that unwanted spurious free waves are generated together with desired free waves (cf. [32, 33]). These components are the sum of the frequencies (superharmonics) or difference of the frequencies (subharmonics). These spurious free waves can be explained by the 2nd-order wave maker theory. In this section, we review the complete 2nd-order flap type wave maker theory derived by Schaffer (1996) [34]. The wave field is assumed to be stationary, which means the wave spectrum does not evolve temporally and spatially. Figure 3 is a sketch of the boundary condition of the problem addressed here.

ζ, ϕ and X denote free surface, velocity potential and displacement of the wave board. ζ, ϕ and $X_0 (= X(z=0))$ are decomposed to 2nd order using a small ordering parameter ϵ :

$$\begin{cases} \zeta = \epsilon \zeta^{(1)} + \epsilon^2 \zeta^{(2)} \\ \phi = \epsilon \phi^{(1)} + \epsilon^2 \phi^{(2)} \\ X_0 = \epsilon X_0^{(1)} + \epsilon^2 X_0^{(2)}. \end{cases} \quad (1)$$

Solving the Laplace’s equation for the boundary condition described in Fig. 3, the 1st-order solution can be obtained:

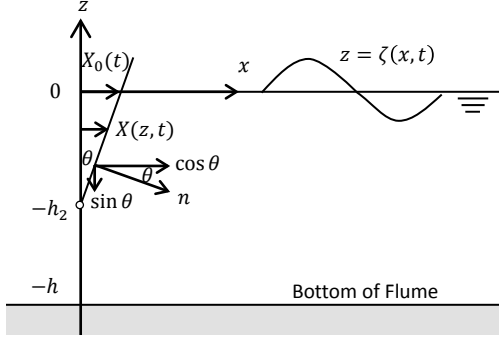


Figure 3. BOUNDARY CONDITION AT THE WAVE BOARD FOLLOWING [33, 34].

$$\zeta^{(1)} = \frac{1}{2} \left\{ X_a \sum_{j=0}^{\infty} c_j e^{i(\omega t - k_j x)} + c.c. \right\}, \quad (2)$$

where ω, k and X_a denote angular frequency, wavenumber and complex amplitude of $X_0^{(1)}$. “c.c.” denotes the complex conjugate. The component with $j = 0$ corresponds to the progressive wave and those with $j \geq 1$ correspond to the evanescent modes. c_0 is the Biesel’s transfer function expressed as

$$c_0(k_0) = \frac{2 \sinh k_0 h (k_0 h_2 \sinh k_0 h - \cos k_0 h + \cosh k_0 (h - h_2))}{k_0 h (k_0 h + \sinh k_0 h \cosh k_0 h)}. \quad (3)$$

The 2nd-order solution is then decomposed to three parts:

$$\zeta^{(2)} = \zeta^{(21)} + \zeta^{(22)} + \zeta^{(23)}. \quad (4)$$

The progressive components of these solutions are described as

$$\begin{cases} \zeta_{nm0}^{(21)\pm} = G_{nm}^{\pm} A_n A_m^{-*} e^{i(\theta_{0n} \pm \theta_{0m}^{\pm})} \\ \zeta_{nm0}^{(22)\pm} = \frac{1}{2} \left\{ \frac{A_n A_m^{-*}}{h} c_0^{(22)\pm} e^{i((\omega_n \pm \omega_m)t - K_0^{\pm})} + c.c. \right\} \\ \zeta_{nm0}^{(23)\pm} = -\zeta_{nm0}^{(22)\pm}. \end{cases} \quad (5)$$

Here, A denotes the complex amplitude of the progressive component of $\zeta^{(1)}$, and n and m are the indices of free wave components. The superscripts $+$ and $-$ represent superharmonics and subharmonics, respectively. The descriptions of other functions or coefficients can be found in [34]. Hereafter, subscript 0 is omitted for brevity. Physical meanings of each solutions in Eqn. (5) are as follows.

$\zeta_{nm}^{(21)\pm}$: Bound waves, which correspond to the 2nd-order solution of the Stokes’ wave (Stokes 1847 [35]).

$\zeta_{nm}^{(22)\pm}$: Spurious free waves, which occur due to the boundary condition of wave board.

$\zeta_{nm}^{(23)\pm}$: The solution to compensate spurious free waves ($\zeta_{nm}^{(22)\pm}$) with the 2nd-order control of the wave board motion ($X^{(2)}$).

Equation (5) shows that $\zeta_{nm}^{(21)\pm}$ and $\zeta_{nm}^{(22)\pm}$ are the components that occur due to the interaction among linear wave solutions $\zeta^{(1)}$. Only $\zeta_{nm}^{(23)\pm}$ is generated by the 2nd-order control of the wave board motion.

HOSM Calculation

In the proposed wave generation method, the input signal is based on HOSM simulation. In HOSM, the following free surface boundary conditions (Eqn. (6)) written in terms of ζ and $\phi^s (= \phi|_{z=\zeta})$ as in [19] are solved numerically.

$$\begin{cases} \zeta_t + \nabla_x \zeta \cdot \nabla_x \phi^s - (1 + \nabla_x \zeta \cdot \nabla_x \zeta) W = 0 \\ \phi_t^s + g \zeta + \frac{1}{2} \nabla_x \phi^s \cdot \nabla_x \phi^s - \frac{1}{2} (1 + \nabla_x \zeta \cdot \nabla_x \zeta) W^2 = 0, \end{cases} \quad (6)$$

where $\nabla_x = (\partial/\partial_x, \partial/\partial_y)$, $W = \phi_z^s$ and g denotes gravitational acceleration. Then, ϕ is expanded to perturbed time series up to the order of nonlinearity M . The spatial derivative is solved efficiently in wavenumber space using the Fast Fourier Transform (FFT). The 4th-order Runge-Kutta method is used for temporal integration.

Initial wave field is given by

$$\begin{cases} \zeta(x) = Re \left[\sum_{m,n} \alpha_{mn} \exp\{i(k_{xm}x + k_{yn}y + \varphi_{mn})\} \right] \\ \phi^s(x) = Re \left[\sum_{m,n} -i \frac{g}{\omega_{mn}} \alpha_{mn} \exp\{i(k_{xm}x + k_{yn}y + \varphi_{mn})\} \right] \\ \left(\alpha_{mn} = \sqrt{2S(k_{xm}, k_{yn}) dk_x dk_y} \right), \end{cases} \quad (7)$$

which is based on the linear wave theory. Here, φ denotes initial wave phase given as a random number in the range of $[0, 2\pi)$. Hereafter, m and n denote the indices of k_x and k_y , respectively. S is wavenumber spectrum. These solutions in Eqn. (7) do not exactly satisfy the fully nonlinear boundary condition in Eqn. (6); therefore, unwanted free standing waves appear in the calculation domain. To prevent this, we adopt the nonlinear wave initialization method proposed by Dommermuth (2000) [36]. In this method, ramp-up function $F(t)$ is multiplied by the nonlinear terms in the perturbation time series as

$$\begin{cases} \zeta_t = w^{(1)} + F(t) \{-\nabla_x \phi^s \cdot \nabla_x \zeta + H.O.T.\} \\ \phi_t^s = -g \zeta + F(t) \left\{ -\frac{1}{2} |\nabla_x \phi^s|^2 + \frac{1}{2} w^{(1)} w^{(1)} + H.O.T. \right\} \\ \left(F(t) = 1 - \exp\left\{-\left(\frac{t}{T_a}\right)^{n_a}\right\} \right), \end{cases} \quad (8)$$

where $H.O.T.$ denotes higher order terms, and n_a and T_a are arbitrary constants. At time $t = 0$, the initial wave

solutions in Eqn. (7) exactly satisfy the boundary condition in Eqn. (8). As F becomes larger with time, the wave field gradually adjusted to nonlinear free surface conditions. This procedure allows us to avoid generating unwanted standing waves and to generate bound waves naturally.

Initialization Of The Wave Field In The Basin

Initial wave fields are given in the HOSM simulation, but wave generation in a wave basin begins from still water. If the signals based on the HOSM simulation are given to all the wave makers in ASMB, the components in the signals that are expected to propagate outward generate unwanted waves propagating inward in the basin at the beginning.

In ASMB, southward propagating unidirectional modulational wave trains, whose spatial periodic boundary in HOSM coincides with North and South wave makers, were reproduced by HOSM-WG in [1]. They concluded that it was enough to give signals only to the upwind side wave makers, and was enough to control downwind side wave makers with absorbing mode only. This control method prevents the downwind side wave makers from generating unwanted waves propagating inward in the basin at the beginning. After the waves propagated from the upwind side reach the downwind side wave makers, the wave makers began to absorb incident waves. This wave maker motion corresponds to that of generating waves that are expected to propagate outward in the basin in the HOSM simulation at this position.

The same applies for the case that the spatial periodic boundary in HOSM does not coincide with wave makers. It is enough to actively/passively absorb incident waves in the downwind side of the wave basin. For the case of directional wave generation, this condition is so interpreted that the components that propagate outward in the basin should be removed for each wave maker signal.

Calculation Of Wave Maker Signal: Unidirectional waves

The calculation procedure of the wave maker signal of HOSM-WG to generate freak waves in unidirectional waves in a wave basin is as follows. Here, waves are assumed to propagate in the direction of $x > 0$.

HOSM simulation. Initial surface elevation $\zeta(x, t = 0)$ and velocity potential $\phi^s(x, t = 0)$ are calculated using Eqn. (2). Then, the nonlinear temporal evolution of the wave field is calculated by HOSM using the Dörmmermuth's initialization scheme (Eqn. (8)). In order to develop the wave modulation sufficiently, we need integration time of $O(\epsilon^{-2}\omega_p^{-1})$ where subscript p denotes the peak component of the waves [2].

Detection of freak waves. The position ($x = x_{fr}$) and the time ($t = t_{fr}$) of the freak wave occurrence in the calculation domain of HOSM are detected. Individual wave heights at every node of the domain are calculated using the zero-up-crossing method; then, the wave that has the maximum wave height (which satisfies $H > 2H_s$) is detected. In some cases, the wave whose crest height is maximal is detected in this study.

Acquisition of the time series of surface elevation at the wave maker position. Here, L_{fr} is defined as the distance between the desired position of freak wave occurrence and the wave board in the wave basin. $L_{fr} = L_{tank}/2$ when we want to generate freak wave at the center of the basin whose length is L_{tank} . Then, the corresponding x -coordinate of the wave maker position is

$$x_{wm} = \text{mod}(x_{fr} - L_{fr}, x_{domain}), \quad (9)$$

where the calculation domain is $0 \leq x \leq x_{domain}$, and $\text{mod}(A, B)$ denotes the remainder of A divided by B . x_{wm} can be defined in the case of $x_{fr} < L_{fr}$ making use of the periodic boundary condition of HOSM calculation domain. Then, the time series of surface elevation at the wave maker position $\zeta(x_{wm}, t)$ is obtained. In addition, the time series is extracted around $t = t_{fr}$ taking into consideration of the following:

- Long-term wave generation causes contamination of the wave field due to reflected waves. The time of the freak wave occurrence from the start of wave generation should be shortened.
- It is also necessary to taking into account of the time to reach $x = x_{fr}$ for the shortest wave component of interest.

Calculation of wave maker signal. The wave board velocity $V(t)$ is calculated as

$$V(t) = F^{-1} \left[\frac{\omega}{c} F[\zeta(x_{wm}, t)] \right], \quad (10)$$

where $F[\]$ and $F^{-1}[\]$ denote FFT and inverse FFT, respectively, and c denotes the Biesel's transfer function c_0 in Eqn. (3).

In order to suppress the modulation of the front of the wave group at the beginning of wave generation and of the rear at the end, the following linear ramp-up and ramp-down functions are multiplied by $V(t)$ for five seconds.

$$f(t) = \begin{cases} t/5, & \text{for } 0 \leq t \leq 5 \\ (t_{end} - t)/5, & \text{for } t_{end} - 5 \leq t \leq t_{end}. \end{cases} \quad (11)$$

The wave energy seems to spread in frequency when the

FFT is applied to $\zeta(x, t)$ because HOSM calculates the temporal evolution of wave field. There exists a little leaked energy around $\omega = 0$. Biesel's transfer function c is 0 at $\omega = 0$, so the small frequency components in $V(t)$ are intensified (Eqn. (10)). To prevent this slow trend on $V(t)$, high-pass filter is applied:

$$HP(\omega) = \begin{cases} 0 & \text{for } |\omega| \leq \omega_{lt} \\ 1 & \text{for } |\omega| \geq \omega_{lt} \end{cases} \quad (12)$$

where ω_{lt} denotes the lower threshold frequency of the filter. In this study, $\omega_{lt} = \omega_p/5$ is chosen, which is in the region of sufficiently small energy in the frequency domain.

Calculation Of Wave Maker Signal: Short-Crested Waves

The calculation procedure of the wave maker signal of HOSM-WG to generate freak waves in short-crested waves in a wave basin is as follows.

Preparation of the directional spectrum. The directional spectrum to be reproduced in a wave basin is prepared first. In this study, both standard spectrum and hindcast spectrum are used. If there is a desired wave field, such as marine accident, the directional spectrum $S(f, \theta)$ is hindcast by the third-generation wave model. Then, the following transformation is applied to $S(f, \theta)$:

- **Coordinate transformation:** Coordinates have to be transformed from (f, θ) to (k_x, k_y) for the HOSM simulation.
- **Scaling:** Taking into account of the size of the wave basin or the model ship size in the case of seakeeping test, the peak wave length has to be adjusted to the experimental scale.
- **Rotation:** Directional spectrum should be rotated so that the peak direction corresponds to the desired direction in the wave basin. In this study, the peak direction is adjusted to southward in ASMB.

HOSM simulation. Initial surface elevation $\zeta(x, t = 0)$ and velocity potential $\phi^s(x, t = 0)$ are calculated using Eqn. (2) in which transformed spectrum $S(k_x, k_y)$ is used. Then, the nonlinear temporal evolution of the wave field is calculated by HOSM in the same way as in the unidirectional wave case.

Detection of freak wave. In the same way as in the unidirectional wave case, the position ($x = x_{fr}$) and the time ($t = t_{fr}$) of the freak wave occurrence are detected from the HOSM simulation output.

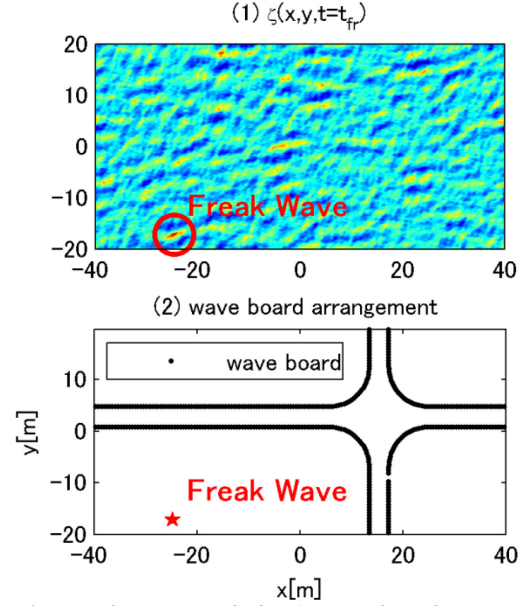


Figure 4. TWO DIMENSIONAL PLOT OF THE WAVE FIELD AT THE INSTANCE OF FREAK WAVE OCCURRENCE IN HOSM CALCULATION (1) AND THE LOCATION OF THE VIRTUAL WAVE MAKERS IN HOSM CALCULATION DOMAIN (2).

Virtual arrangement of wave makers in the HOSM calculation domain. In this study, the experiments of freak wave generation in short-crested waves are conducted in ASMB, and the freak wave is adjusted to appear in the center of ASMB. The top panel of Fig. 4 shows the spatial wave form at the instance of freak wave occurrence in the HOSM simulation. The location of the virtual wave maker is adjusted in the HOSM calculation domain so that the freak wave appears in the center of ASMB. Here, the calculation domain (80 m \times 40 m) is at the same scale as the size of ASMB, the virtual wave maker position is determined as in the bottom panel of Fig. 2, making use of the periodic boundary condition of HOSM.

Calculation of the transfer function. The transfer function for directional wave can be expressed as in Eqn. (13), which is derived from the energy flux conservation (cf. [37]).

$$c'(k_{mn}, \beta_{mnq}) = \frac{c(k_{mn})}{\cos \beta_{mnq}} \quad (13)$$

$$\text{here, } \begin{cases} \beta_{mnq} = \theta_{mn} - \theta_q \\ k_{mn} = \sqrt{k_{xm}^2 + k_{ym}^2} \\ \theta_{mn} = \arctan(k_{ym}/k_{xm}), \end{cases}$$

where q, θ_{mn} and θ_q denote the index of wave makers, the direction of the wave component of (k_{xm}, k_{ym}) and the direction of wave maker q . At each time step, for each q the

matrix of surface elevation in wavenumber space $\hat{\zeta}(k_x, k_y)$ is multiplied by the matrix $|\omega_{mn}|/c'_{mn;q}$, and then the inverse FFT is applied. The following filter is applied to this matrix $|\omega_{mn}|/c'_{mn;q}$:

- Removal of outward propagating components for each wave maker.

As mentioned before, the components that propagate outward in the basin for each wave maker should be removed during the initialization of the wave fields. This condition can be expressed as

$$\cos \beta_{mnq} < 0. \quad (14)$$

- Biesel's limit

In the case of unidirectional wave generation, evanescent modes appear due to the difference of vertical profile between wave board configuration and the horizontal particle velocity of the wave (see Eqn. (2)). Similarly, in the case of directional wave generation, evanescent modes appear due to the difference of horizontal profile between them. A practical method to make the longest wave of the latter type of evanescent modes decay at the length scale of $O(\lambda_p)$ was proposed by Biesel (1954) [38], which removes the components expressed by

$$\sin|\beta_{mnq}| > \frac{2\pi}{k_{mn}d} - \sqrt{2}, \quad (15)$$

where d denotes the width of wave board.

- Removal of the component of $\mathbf{k} = \mathbf{0}$

In order to prevent the divergence of the calculation of $V(t)$, the component of $\mathbf{k} = \mathbf{0}$ should be removed because $c'(\mathbf{k} = \mathbf{0}) = 0$.

Calculation of wave maker signal. Wave maker signal is calculated using the transfer function c' obtained in the previous section. In the surface elevation in wavenumber space $\hat{\zeta}(\mathbf{k}, t)$ output from HOSM, we cannot distinguish the component of $+\mathbf{k}$ from that of $-\mathbf{k}$ because $\hat{\zeta}(\mathbf{k}, t)$ is calculated as the spatial FFT of $\zeta(x, y, t)$. The separated Fourier component $\hat{\zeta}_{sep}(\mathbf{k}, t)$ can be calculated using the velocity potential $\widehat{\phi}^s(\mathbf{k}, t)$ as below:

$$\hat{\zeta}_{sep}(\mathbf{k}, t) = \hat{\zeta}(\mathbf{k}, t) + \frac{i\omega}{g} \widehat{\phi}^s(\mathbf{k}, t). \quad (16)$$

Equation (16) is based on the linear wave theory. The wave board velocity $V(x, y; t, q)$ at the time t for the wave board q is calculated using $\hat{\zeta}_{sep}(\mathbf{k}, t)$ as

$$V(x, y; t, q) = F_{xk}^{-1} \left[\frac{\omega_{mn}}{c'_{mnq}} \hat{\zeta}_{sep}(\mathbf{k}_{mn}, t) \right], \quad (17)$$

where F_{xk}^{-1} denotes inverse spatial FFT. This is a value on the calculation node, so applying bi-cubic interpolation, the velocity of each wave maker $V(x_q, y_q, t)$ is calculated.

Improvement Of HOSM-WG

In this section, three improvement methods of HOSM-WG are proposed. The effectiveness of these methods will be discussed in **Effects Of Improved Methods**.

Method I: Separation Of Free Waves From Bound Waves.

ζ and ϕ^s output from the HOSM simulation includes bound waves. When the wave maker signal is calculated by Eqn. (10) or Eqn. (17) in these HOSM solutions, the bound wave components of HOSM are inadvertently generated as free waves in the basin. Only the free wave components should be included in the wave maker signals. Here, the method of free wave separation using the wavenumber-frequency spectrum proposed in [39] is used.

Figure 5 shows the examples of the wavenumber-frequency spectra of modulational wave train (1) and unidirectional irregular wave (2) in the HOSM simulations. We can see that the energy of free waves and that of bound waves distribute separately in the wavenumber-frequency space. For the modulational wave trains, we can also see that the free wave energy distributes along the straight line, which is tangent to the linear dispersion relation curve at the peak wavenumber (Fig. 5 (1)). Similar figure can be found in [40, 41], and these authors noted that this deviation is caused by the temporal phase evolution, which is due to quasi-resonant interaction. In the case of unidirectional irregular waves in this study, this kind of deviation is not obvious (Fig. 5 (2)). Then, the filter that covers the region of the tangential line to the dispersion relation curve is applied for modulational wave trains and the filter that covers the region around the linear dispersion relation curve is applied for unidirectional irregular waves so that only the free wave components are extracted.

Method II: Using Biesel's Transfer Function In Wavenumber Space.

It is obvious from Fig. 5 that the wave spectrum obtained from the HOSM simulation is broad in frequency because the wave evolves in time. Moreover, as is mentioned in the previous section, the energy distribution region deviates from the linear dispersion relation curve for the modulational wave trains. On account of these facts, the transfer function should be applied not in frequency space but in wavenumber space. (Transfer function has already been applied in wavenumber space for short-crested waves (Eqn. (13)).)

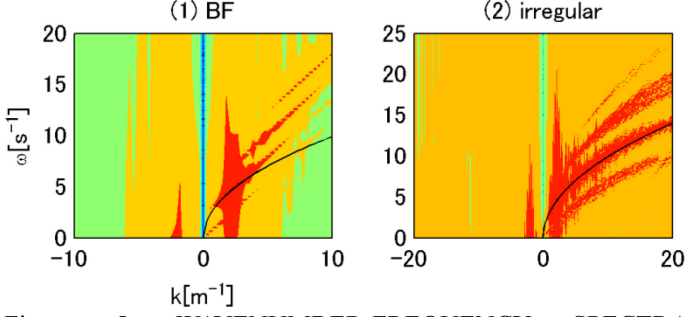


Figure 5. WAVENUMBER-FREQUENCY SPECTRA $\zeta(k, \omega)$ FROM HOSM SIMULATION OF MODULATIONAL WAVE TRAIN (1) AND UNIDIRECTIONAL IRREGULAR WAVE (2). BLACK CURVE SHOWS THE LINEAR DISPERSION RELATION.

Method III: Using Schaffer's 2nd-Order Wave Maker Control Method. Even if the free waves are separated from bound waves in the output of the HOSM simulation in Method I, spurious free waves are generated ($\zeta^{(22)}$ in Eqn. (5)). To prevent this, the 2nd-order wave maker control ($X^{(2)}$) is applied. Detail description of $X^{(2)}$ can be found in [34]. As mentioned in [34], there exists singularity at $\omega_m = 2\omega_n$ in the calculation of subharmonics, so these components are ignored here. In the calculation of $X^{(2)}$, evanescent modes are taken into account up to the 50th component.

VALIDATION OF HOSM-WG

Methods

Experiments in ASMB and WT and numerical experiments using 2-dimensional fully nonlinear numerical wave tank were carried out. The measured time series of surface elevation are compared with corresponding ones by HOSM simulations.

Experiments In Wave Basin. In ASMB, modulational wave trains, freak waves in unidirectional irregular waves and freak waves in short-crested irregular waves were generated. In WT, modulational wave trains and freak waves in unidirectional irregular waves were generated. Time series of the surface elevation were measured by capacitance wave gauges, which were deployed in these basins (Fig. 1 and Fig. 2). Wave maker signals were calculated so that the desired freak waves would appear at the center of ASMB or at the position of the wave gauge #7 in WT.

Numerical Experiments With NWT2D. Fully nonlinear computation with 2-dimensional numerical wave tank was carried out. Here, the fully nonlinear solver based on

boundary element method, called NWT2D, developed by Tanizawa (1996) [42] is used. NWT2D models the exact geometry of the WT, including the shape and motion of the flap. Direct comparison of the time series of surface elevation between WT experiment and NWT2D simulation is possible up to the time of wave breaking occurrence.

Comparison. The time series of surface elevation $\zeta(t)$ obtained from HOSM simulation and from HOSM-WG experiments in the wave basin and from numerical HOSM-WG experiments with NWT2D are compared. Correlation coefficient r and root mean square error $RMSE$ are evaluated. The definitions of r and $RMSE$ are as follows:

$$r = \frac{\sum_{j=1}^N (x_j y_j)}{\sqrt{\sum_{j=1}^N (x_j^2)} \sqrt{\sum_{j=1}^N (y_j^2)}}, \quad (18)$$

$$RMSE = \frac{\sqrt{(\sum_{j=1}^N (y_j - x_j)^2)/N}}{4\sqrt{m_0}}, \quad (19)$$

where $x_j = x(t_j)$ and $y_j = y(t_j)$ denote the time series of surface elevation used in the comparison, and N denotes the number of the data used for the comparison. Here, $RMSE$ is normalized with $4\sqrt{m_0}$, which corresponds to significant wave height H_s . $\sqrt{m_0}$ can be calculated as

$$\sqrt{m_0} = \sqrt{(\sum_{j=1}^N (y_j - \bar{y})^2)/N} \sim \frac{H_s}{4}. \quad (20)$$

Modulational Wave Trains

Modulational wave trains were reproduced well by HOSM-WG in ASMB [1]. It has also been shown that the difference between HOSM-WG experiments and HOSM simulation becomes large when the modulation is the largest. Here, we show the effect of improved HOSM-WG, spatial periodicity of HOSM-WG, the effect of the order of nonlinearity of HOSM, and the effect of wave steepness.

Initial wave form used in HOSM simulation is given by

$$\zeta(x) = a_c \cos(k_c x) + b_+ \cos(k_+ x + \varphi_+) + b_- \cos(k_- x + \varphi_-), \quad (21)$$

where subscripts c , $+$ and $-$ denote the carrier wave component, upper sideband component and lower sideband component, respectively, $k_{\pm} = k_c \pm \Delta k$ (Δk : perturbation wavenumber), φ_{\pm} denotes the initial phase of sidebands. φ_{\pm} and b_{\pm}/a_0 are set to $-\pi/4$ and 0.1 with $a_0 = (a_c^2 + b_+^2 + b_-^2)^{1/2}$.

The number of nodes of the calculation domain $N_x = 512$ was used in the HOSM simulation. The time step $\Delta t = 0.02$

Table 1. IMPROVED METHOD OF HOSM-WG AND ESTIMATED VALUES OF r AND $RMSE$. SYMBOLS ARE: \circ , APPLIED; \times , NOT APPLIED.

Improving method			evaluated values	
I	II	III	r	$RMSE$
\times	\times	\times	0.965	0.0659
\circ	\times	\times	0.984	0.0455
\circ	\circ	\times	0.988	0.0389
\circ	\circ	\circ	0.989	0.0371

$sec (\sim T_c/80)$ was used in HOSM simulation for the experiments in ASMB and $\Delta t = 0.005 sec (\sim T_c/277)$ for the experiments in WT, where T_c denotes the carrier wave period. For stability of the calculation, Δk was set at twice of the minimal wavenumber dk of the HOSM simulation. Therefore, only two same wave groups exist in the calculation domain of HOSM. Other parameters of modulational wave trains and of the HOSM simulation will be explained in detail below.

Effects Of Improved Methods. Modulational wave trains with a carrier wave length $\lambda_c = 3.0 m$, initial wave steepness $a_0 k_c = 0.101$ and the number of waves in a wave group in space $N_k (= k_c/\Delta k) = 7$ were used here. The HOSM simulation was carried out with the order of nonlinearity $M = 5$, and $T_a/T_c = 12$ and $n_a = 4$ in the ramp-up function $F(t)$ in Eqn. (8). Wave maker signals were calculated for each of the improved methods. The HOSM-WG experiments were conducted numerically with NWT2D.

Mean and standard deviation of r and $RMSE$ at the 13 wave gauges (#1 to #13) are shown with improved methods in Tab. 1. The data in the range of $t_{max} - N_k T_c \leq t \leq t_{max} + N_k T_c$ is used for analysis, where t_{max} denotes the time of the largest modulation. The difference between HOSM-WG experiment and HOSM simulation becomes smaller as more improved methods are included. All the proposed improved methods, especially methods I and II, are effective at improving HOSM-WG.

Spatial Periodicity. Generated waves with HOSM-WG should be periodic in space because spatial periodic boundary condition is imposed on HOSM. Modulational wave trains with $\lambda_c = 3.0 m$, $a_0 k_c = 1/12$ and $N_k = 6$ were generated by HOSM-WG method with NWT2D. The HOSM simulation was carried out with $M = 5$, $T_a/T_c = 12$ and $n_a = 4$. All three improved methods were adopted. The time series of surface elevation measured at $x = 9 m$ and at $x = 27 m$ are shown in Fig. 6. These two measuring points are separated by just one wave group length. These two time series show an excellent agreement after the wave group reaches $x = 27 m$. The configurations of the three wave groups shown in Fig. 6 are slightly different, which

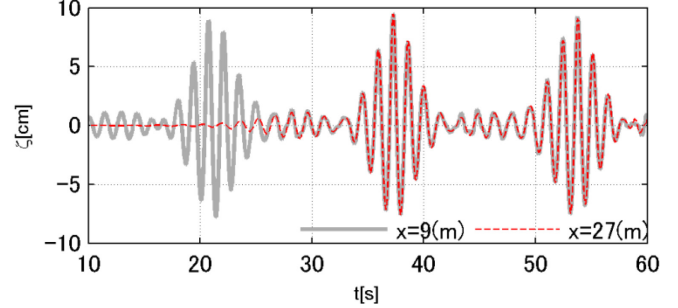


Figure 6. TEMPORAL EVOLUTION OF MODULATIONAL WAVE TRAIN AT $x = 9(m)$ (GRAY) AND AT $x = 27(m)$ (RED) IN NWT2D EXPERIMENT.

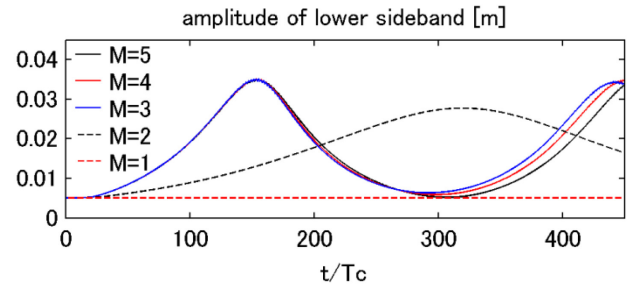


Figure 7. TEMPORAL EVOLUTION OF LOWER SIDEBAND AMPLITUDE OF THE BF WAVE TRAIN WITH THE ORDER OF NONLINEARITY M FROM 1 TO 5 IN HOSM SIMULATION.

indicates that the waves evolve in time. It is confirmed that the generated waves with HOSM-WG behaves periodic in space and aperiodic in time.

Effects Of The Order Of Nonlinearity On HOSM.

Modulational wave trains with $\lambda_c = 4.0 m$, $a_0 k_c = 0.080$ and $N_k = 9$ were used here. HOSM-WG experiments with M from 1 to 5, $T_a/T_c = 20$ and $n_a = 4$ were conducted in ASMB. No improved methods were applied in the calculation of wave maker signals.

The temporal evolution of the lower sideband in the HOSM simulation with M from 1 to 5 is shown in Fig. 7. Little difference among $M = 3 - 5$ can be seen up to the time of the largest modulation. No evolution can be seen with $M = 1$ because this corresponds to the linear wave simulation. The slower evolution can be seen with $M = 2$ even though (quasi-)resonant interaction is a phenomenon due to 3rd-order nonlinearity. This indicates that the order of nonlinearity in HOSM M is not the same as that in Stokes wave theory [10]. Using these HOSM outputs, the HOSM-WG experiment was conducted. Measured surface elevation time series at each wave gauge were compared with those from the HOSM simulation, and then the values of r and $RMSE$ were evaluated. The HOSM-WG experiment results with

Table 2. EVALUATED VALUES OF r AND $RMSE$ BETWEEN HOSM SIMULATION AND HOSM-WG EXPERIMENT.

M of HOSM-WG	sim.	evaluated values		symbols in Fig. 8
		r	$RMSE$	
1	1	0.998	0.0341	
2	2	0.985	0.0500	
3	3	0.967	0.0682	Δ
4	4	0.970	0.0650	\square
5	5	0.976	0.0608	\times
1	5	0.253	0.312	
2	5	0.772	0.165	
3	5	0.975	0.0610	\blacktriangledown
4	5	0.974	0.0603	\blacklozenge

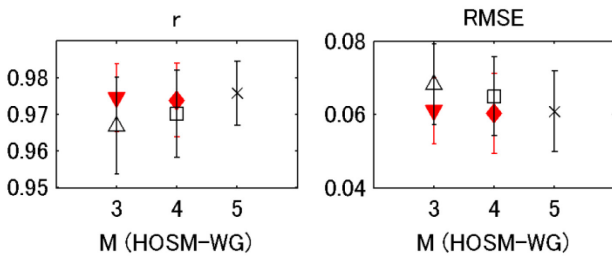


Figure 8. EVALUATED VALUES OF r AND $RMSE$ BETWEEN HOSM SIMULATION AND THE HOSM-WG EXPERIMENT. SYMBOLS ARE DEFINED IN Tab. 2.

$M = 1 - 4$ were also compared with those of the HOSM simulation with $M = 5$.

Mean and standard deviation of r and $RMSE$ at the 18 wave gauges are listed in Tab. 2. These values of the cases with $M \geq 3$ for HOSM-WG are plotted against M of HOSM-WG in Fig. 8. Comparison between HOSM-WG experiment and HOSM simulation with the same M shows that the difference between them becomes smaller as M becomes larger for $M \geq 3$. It can also be seen that the HOSM-WG experiments with $M = 3, 4$ agree better with the HOSM simulation with $M = 5$ than that with the same M . Possible reason of these results is as follows.

Figure 7 suggests that there is little difference among $M = 3 - 5$ in the evolution of free wave components up to the time of the largest modulation. In each case, bound waves that correspond to $M = \infty$ should be naturally generated from the free waves in the experiments. Therefore, experiments show a better agreement with HOSM simulation when taking into account of higher order of nonlinearity.

For $M = 1, 2$, an excellent agreement can be seen between HOSM-WG experiment and HOSM simulation with the same M because there is little evolution of modulation in the spatial scale of the basin $O(\epsilon^{-1}k_c^{-1})$. However, the HOSM simulation with $M = 1, 2$ cannot reproduce the actual free wave evolution in time, so the experiments do not agree at all with the simulation of $M = 5$.

The scale of the nonlinear evolution of modulational wave train is $O(\epsilon^{-2}\omega_c^{-1})$ or $O(\epsilon^{-2}k_c^{-1})$. However, in HOSM-WG because the nonlinear evolution in the time scale of $O(\epsilon^{-2}\omega_c^{-1})$ is calculated in advance, the large wave based on the process of quasi-resonant interaction can be reproduced in the basin of the spatial scale $O(\epsilon^{-1}k_c^{-1})$.

Effects Of Wave Steepness. Here, the steepness is defined as a_0k_c , where a_0 expresses the total energy of this wave system and k_c expresses the carrier wavenumber. Total energy a_0 is invariant in time. The steepness a_0k_c represents the nonlinearity of the wave system.

Modulational wave trains with $\lambda_c = 3.0 m$, $a_0k_c = 0.08 - 0.115$ and $N_k = 7$ were used here. An HOSM simulation was carried out with $M = 5$, $T_a/T_c = 12$ and $n_a = 4$. All three improved methods were applied in the calculation of wave maker signals. The HOSM-WG experiments were conducted in WT and were also numerically conducted with NWT2D.

Wave breakings (or divergence of calculation) were observed for $a_0k_c \geq 0.1015$ in the WT experiments, and for $a_0k_c \geq 0.109$ in the NWT2D experiments. This fact indicates that HOSM overlooks wave breaking to some extent, which was noted in [43, 44]. Unfortunately, the flap motion in WT turned out to be slightly larger than the given signal value. Therefore, wave breakings were observed for smaller value of a_0k_c in the WT experiments than in the NWT2D experiments.

Evaluated r and $RMSE$ are plotted against a_0k_c in Fig. 9. Only the non-breaking cases are plotted for the NWT2D experiments. Figure 9 clearly shows that the difference between HOSM-WG experiment and HOSM simulation becomes larger as wave steepness a_0k_c becomes larger. However, r is larger than 0.95 and $RMSE$ is smaller than 0.08 even for the wave breaking cases; so it can be said that HOSM outputs are reproduced well in the basin as a whole by HOSM-WG. Figure 9 also indicates that the HOSM output was reproduced better in the WT experiments than in the NWT2D experiments in spite of larger motion of the flap in the NWT2D experiments. The possible causes of this are as follows.

- There exists some overlap of the energy distribution region between free waves and bound waves in the wavenumber-frequency space (see Fig. 5). There is some possibility that the energy of free waves is partially removed when the filter is applied in the improved method I.
- As wave breaking appears in the HOSM-WG experiments, HOSM cannot correctly express the locally highly nonlinear area of the wave trains. Some inaccuracy around the large wave crest can arise due to the assumption of the single-valued function of free surface ζ on x or the truncation of higher order terms in HOSM.

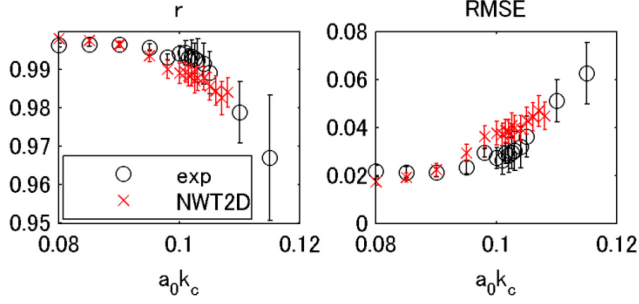


Figure 9. EVALUATED VALUES OF r AND $RMSE$ BETWEEN HOSM SIMULATION AND EXPERIMENTS WITH INITIAL WAVE STEEPNESS $a_0 k_c$ FROM 0.08 TO 0.115. \circ : EXPERIMENTS AT WT ; \times : NUMERICAL EXPERIMENTS WITH NWT2D.

Unidirectional Irregular Waves

Calculation Condition Of HOSM. JONSWAP frequency spectrum was used for the initial wave condition of HOSM simulation:

$$S(f) = \frac{\alpha g^2}{(2\pi)^4 f^5} \exp\left\{-1.25 \left(\frac{f_p}{f}\right)^4\right\} \gamma \exp\left\{\frac{(f/f_p - 1)^2}{2\sigma^2}\right\} \quad (22)$$

$$\left(\sigma = \begin{cases} 0.07 & (f \text{ or } f < f_p) \\ 0.09 & (f \text{ or } f > f_p) \end{cases} \right),$$

where f denotes frequency. The parameters α and γ used for the HOSM simulation are listed in Tab. 3 for ASMB experiments and in Tab. 4 for WT experiments. Related parameters, wave steepness $a_0 k_p$ and frequency bandwidth $\Delta f/f_p$, are also listed in these tables. Here, Δf is defined as halfwidth at the half maximum of the frequency spectrum and a_0 is defined as

$$a_0 = 2\sqrt{m_0} \quad \left(m_0 = \int S(f) df \right), \quad (23)$$

which corresponds to a half of the significant wave height.

For cases L1-L6, the HOSM simulation of the unidirectional irregular waves with $\lambda_p = 4.0 m$ was conducted with $M = 5$, $T_a/T_p = 20$, $n_a = 4$, $N_x = 512$, $dk = k_p/18$, and $\Delta t = 0.02 sec$ ($\sim T_p/80$) up to the time $t/T_p = 562$. Three simulations with different random initial phases were carried out for each case (except only two simulations for case L4). A freak wave that had the maximum wave height was detected in each simulation. HOSM-WG experiments were conducted to reproduce these freak waves at the center of ASMB. No improved methods were applied in the calculation of wave maker signals.

For cases L7-L11, the HOSM simulation of the unidirectional irregular waves with $\lambda_p = 3.0 m$ was conducted

Table 3. PARAMETERS OF JONSWAP SPECTRUM USED FOR HOSM-WG EXPERIMENTS IN ASMB.

case	L1	L2	L3	L4	L5	L6
α	0.011	0.0037	0.0080	0.0027	0.0050	0.0017
γ	3.0	20	3.0	20	3.0	20
$a_0 k_p$	0.11	0.11	0.097	0.097	0.076	0.076
$\Delta f/f_p$	0.10	0.057	0.10	0.057	0.10	0.057

Table 4. PARAMETERS OF JONSWAP SPECTRUM USED FOR HOSM-WG EXPERIMENTS IN WT.

case	L7	L8	L9	L10	L11
α	0.012	0.0085	0.0061	0.0045	0.0029
γ	1.0	3.0	6.0	10	20
$a_0 k_p$	0.10	0.10	0.10	0.10	0.10
$\Delta f/f_p$	0.29	0.10	0.075	0.065	0.057

with $M = 5$, $T_a/T_p = 12$, $n_a = 4$, $N_x = 1024$, $dk = k_p/16$, and $\Delta t = 0.005 sec$ ($\sim T_p/277$) up to the time $t/T_p = 187$. Five simulations with different random initial phases were carried out for each case (except only three simulations for case L9). A freak wave that had the maximum wave crest was detected in each simulation. HOSM-WG experiments were conducted to reproduce these freak waves at the position of the wave gauge #7 in the WT. All three improved methods were applied in the calculation of wave maker signals.

Results Of Experiments. Figure 10 shows the freak wave time series of HOSM simulation and HOSM-WG experiment for one of the cases L1 and L2. Good agreement can be seen for both L1 and L2. In particular, the freak wave phases agree well. Figure 11 shows the frequency spectra of the same case of L1 as shown in Fig. 10. Of course, the HOSM simulation (denoted as ‘‘HOSM_num’’) and HOSM-WG experiment (denoted as ‘‘HOSM_WG’’) show a good agreement because their time series are in good agreement. In these spectra, anomalous peaks appear slightly higher or slightly lower than the peak frequency (denoted as ‘‘u’’ for upper/higher and ‘‘l’’ for lower in Fig. 11). The spectrum of the wave generated by the conventional method based on the linear wave theory (Eqns. (2) and (3)) with the frequency spectrum of L1 is also shown in Fig. 11 (denoted as ‘‘Linear_WG’’). In this spectrum, anomalous peaks seen in HOSM_num and HOSM_WG are absent. The difference between these anomalous peak frequencies and peak frequencies can be estimated as $\Delta f_a/f_p = 0.116 \sim O(a_0 k_p)$, where $\Delta f_a = f_u - f_p = f_p - f_l$. This suggests the modulational instability phenomenon in the unidirectional irregular wave train. From the result, freak waves based on the physical process of modulational instability can be reproduced in the basin of the spatial scale of $O(\epsilon^{-1} k_p^{-1})$.

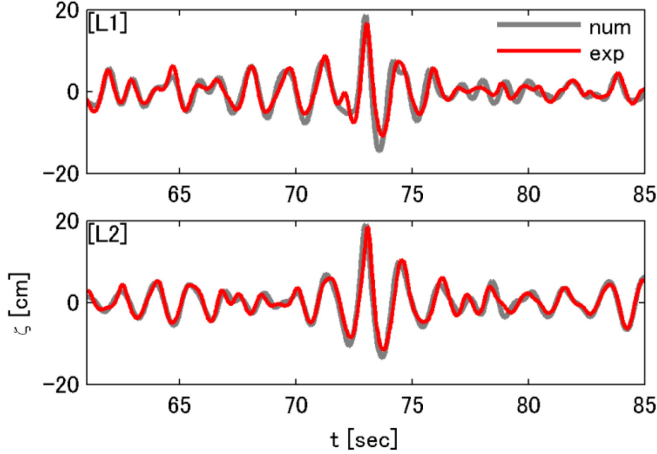


Figure 10. TIME SERIES OF FREAK WAVES FROM HOSM SIMULATION (GRAY) AND EXPERIMENTS (RED): CASE L1 (TOP) AND CASE L2 (BOTTOM).

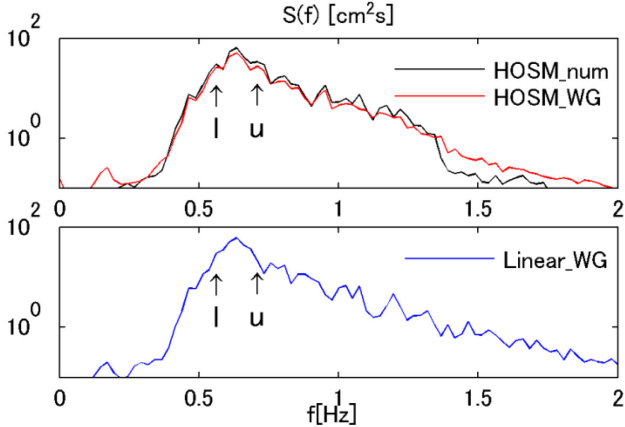


Figure 11. FREQUENCY SPECTRA OF SURFACE ELEVATION RECORDS (CASE L1) FROM THE HOSM SIMULATION (HOSM_num), THE HOSM-WG EXPERIMENT (HOSM_WG) AND THE CORRESPONDING EXPERIMENT WITH CONVENTIONAL WG METHOD (Linear_WG).

The absence of the anomalous peaks in frequency spectrum of Linear_WG suggests that the modulation does not evolve much in the spatial scale of $O(\epsilon^{-1}k_p^{-1})$.

Mean and standard deviation of r and $RMSE$ among 2 – 5 simulations for each case are plotted against frequency bandwidth $\Delta f/f_p$ in Fig. 12. The data in the range of $t_{fr} - (k_p/dk)T_p \leq t \leq t_{fr} + (k_p/dk)T_p$ is used for analysis. It is clearly shown that the difference between HOSM-WG experiment and HOSM simulation becomes larger as $\Delta f/f_p$ becomes larger. It can also be seen from the result of experiment in the ASMB that the difference becomes larger as steepness a_0k_p becomes larger, which indicates modulational wave train.

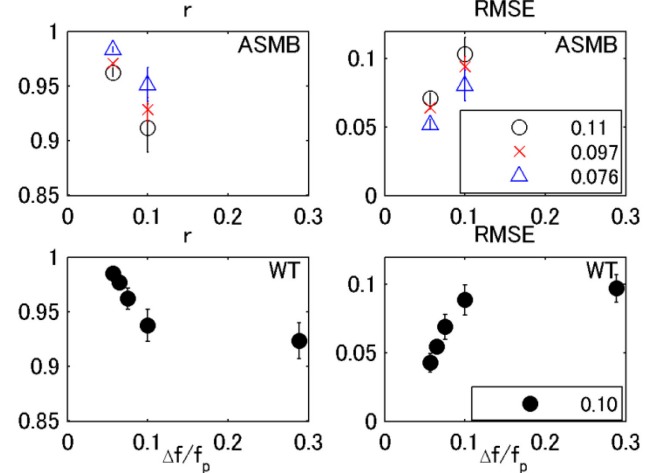


Figure 12. EVALUATED VALUES OF r AND $RMSE$ BETWEEN HOSM SIMULATION AND EXPERIMENTS PLOTTED AGAINST $\Delta f/f_p$. LEGENDS ARE THE VALUES OF WAVE STEEPNESS a_0k_p .

Short-Crested Irregular Waves

Calculation Condition Of HOSM. Two freak waves were observed in the Northwest Pacific Ocean in October 2009 in the point-positioning GPS-based wave measurements [45, 46]. The directional spectra of these events hindcast by the third-generation wave model, WAVEWATCH III, are shown in Fig. 13. These spectra have already been transformed to the wavenumber space, scaled and rotated. Monte-Carlo simulation with these spectra using HOSM and the analysis of the spatial form of freak waves were conducted by [10], which indicated that a freak wave due to modulational instability occurred in case S1 and one due to linear focusing occurred in case S2. Here, these directional spectra are used as the initial wave condition of the HOSM simulation.

Standard spectra were also used here. JONSWAP frequency spectrum (case L1) and the directional distribution function below were adopted:

$$G(\theta) = B \cos^s(\theta/2), \quad (24)$$

where B denotes a normalized factor. Parameters of these freak waves and the time of the freak wave occurrence in the HOSM simulation are listed in Tab. 5. σ_θ denotes the directional spreading [47] defined as

$$\sigma_\theta = \sqrt{2 \left(1 - \sqrt{(a^2 + b^2)/m_0^2} \right)} \quad (25)$$

$$\left(\begin{matrix} a \\ b \end{matrix} \right) = \int_0^{2\pi} \int_0^\infty \begin{pmatrix} \cos \theta \\ \sin \theta \end{pmatrix} S(\omega, \theta) d\omega d\theta.$$

The HOSM simulation of the short-crested irregular waves

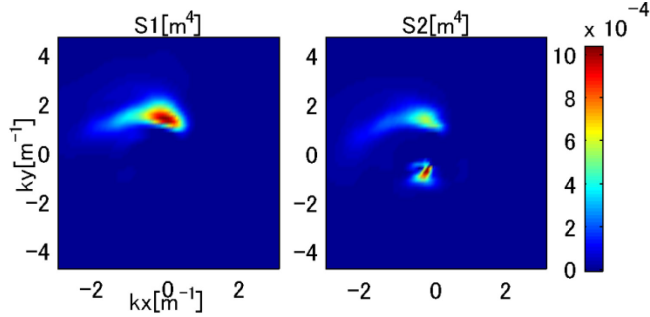


Figure 13. HINDCAST DIRECTIONAL SPECTRA WHEN FREAK WAVE WAS OBSERVED.

Table 5. PARAMETERS OF DIRECTIONAL SPECTRA AND THE TIME OF THE FREAK WAVE OCCURRENCE IN HOSM SIMULATION.

case	Observation		Standard		
	S1	S2	S3	S4	S5
$a_0 k_p$	0.12	0.11	0.11	0.11	0.11
s	-	-	2	10	100
$\sigma_\theta [deg]$	29	53	57	33	11
t_{fr}/T_p	46	54	52	67	47

with $\lambda_p = 4.0 m$ was conducted with $M = 5$, $T_a/T_p = 6$, $n_a = 2$, $N_x \times N_y = 512 \times 512$, $dk_x = k_p/20$, $dk_y = k_p/10$, and $\Delta t = 0.01 sec$ ($\sim T_p/160$) up to the time $t/T_p = 75$. Here, the same coordinate system as the ASMB (Fig. 1) is adopted. Just one freak wave for S1 to S5 was reproduced in the ASMB. No improved methods were applied in the calculation of wave maker signals.

In the preliminary experiments of oblique regular wave generation, it was found that the amplitude of the generated wave became smaller than the one estimated by the transfer function (Eqn. (13)) as the angle of wave propagation $|\beta|$ increased. It appears that this amplitude reduction is caused partially by the unsmoothed boundary condition at the wave makers due to the finite width of the flaps (cf. [38]). In order to improve the wave generation, the transfer function was empirically modified to amplify the component of larger $|\beta|$ of the wave maker signal:

$$c'_{mod}(k, \beta) = \frac{c(k)}{\sqrt{\cos \beta}} \quad (26)$$

This empirically modified transfer function was applied in case S1. This case is denoted as ‘‘S1_mod’’ hereafter.

Results Of Experiments. Figure 14 shows the freak wave time series of HOSM simulation and HOSM-WG experiment for S1, S1_mod and S2. It can be seen that HOSM simulation and HOSM-WG agree well. As is shown

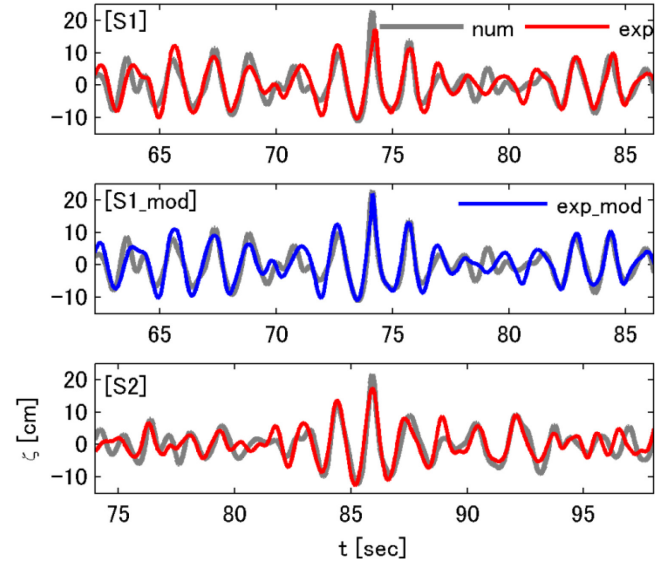


Figure 14. TIME SERIES OF FREAK WAVES FROM HOSM SIMULATION (GRAY) AND FROM EXPERIMENTS (RED OR BLUE).

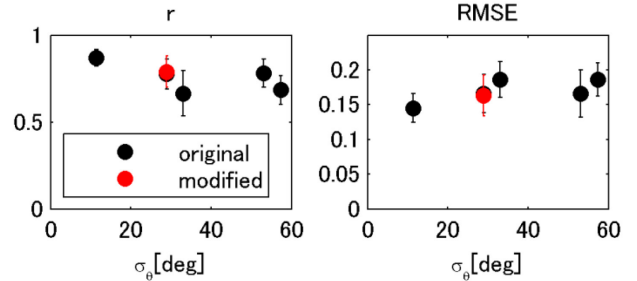


Figure 15. EVALUATED VALUES OF r AND $RMSE$ BETWEEN HOSM SIMULATION AND EXPERIMENTS PLOTTED AGAINST σ_θ .

in Fig. 13, two wave systems exist in the wave field of S2. The angle between them is almost 180° . It is difficult to reproduce such a crossing wave field in an experimental wave basin without equipping wave makers in all sides of the basin. In this respect, this success in reproducing the crossing wave field of S2 is an excellent result. Comparing S1 and S1_mod in Fig. 14, we can see that the accuracy in reproducing freak wave crest is improved as a result of empirical modification of the transfer function.

Mean and standard deviation of r and $RMSE$ at the 18 wave gauges are plotted against the directional spreading σ_θ in Fig. 15. The data in the range of $t_{fr} - 15 \leq t \leq t_{fr} + 15 (sec)$ is used for analysis (except $t_{fr} - 15 \leq t \leq t_{fr} + 10 (sec)$ for S4). It indicates that the difference between HOSM-WG experiment and HOSM simulation becomes larger as directional spreading σ_θ becomes larger. A slight improvement as the result of empirical modification of the transfer function can be seen.



Figure 16. SPATIAL WAVE FORM AT THE INSTANCE OF FREAK WAVE OCCURRENCE FROM THE PICTURE OF EXPERIMENTS (TOP) AND FROM THE HOSM SIMULATION (BOTTOM).

Spatial wave forms at the instance of freak wave occurrence were compared between HOSM simulation and HOSM-WG experiment for S1_mod in Fig. 16. This was just a rough comparison, but the agreement of some geometrical features between them can be ascertained.

CONCLUSION AND FUTURE WORK

The HOSM-WG method for unidirectional irregular waves and short-crested irregular waves is developed, and some improved methods for wave generation are proposed. Wave generation experiments with HOSM-WG were conducted in ASMB, WT and NWT2D. Freak waves in short-crested irregular waves that was detected in the HOSM simulation was successfully reproduced in the ASMB. It is clear that freak waves based on the nonlinear process of quasi-resonant interaction can be reproduced in the basin whose spatial scale is $O(\epsilon^{-1}k_p^{-1})$ by calculating the wave maker signal based on HOSM simulation output. Effectiveness of the improved methods of HOSM-WG and the empirical modification of the transfer function were also ascertained. It was clarified that the difference between HOSM-WG experiment and HOSM simulation became larger as wave steepness, frequency bandwidth of the spectrum or the directional spreading became larger. Further experimental validation of HOSM-WG, especially for short-crested waves, needs to be conducted.

This HOSM-WG method can be used for seakeeping test investigating the structural and motion responses of the ship to freak waves. For such investigation, it is of great importance to clarify their local features such as geometry or kinematics. Visualization of the freak waves generated in experimental wave basin by Particle Tracking Velocimetry and the

investigation of the local features of such waves are on the way and will be reported in future.

ACKNOWLEDGMENTS

The basis of the HOSM numerical solver was provided by Dr. Alessandro Toffoli, which is greatly appreciated. We thank Dr. Wooyoung Choi for useful discussion on the wave generation method based on HOSM simulations. We also thank Mr. Hiroshi Sawada for his assistance in conducting experiments. This work was supported partially by JSPS KAKENHI (Grant Number 25249126), and by the Sasakawa Scientific Research Grant from the Japan Science Society.

REFERENCES

- [1] Waseda, T., Houtani, H. and Tanizawa, K., 2013. "On the generation of spatially periodic breather in a wave tank". In OMAE 2013 – 32nd International Conference on Ocean, Offshore and Arctic Engineering. OMAE2013-10940.
- [2] Janssen, P.A.E.M. 2003. "Nonlinear four-wave interactions and freak waves". *J. Phys. Oceanogr.*, 33, pp. 863-884.
- [3] Onorato, M., Osborne, A.R., Serio, M. et al., 2004. "Observation of strongly non-Gaussian statistics for random surface gravity waves in wave flume experiments". *Phys. Rev. E*, 70, 067302(pp. 1-4).
- [4] Mori, N. and Janssen, P.A.E.M., 2006. "On kurtosis and occurrence probability of freak waves", *J. Phys. Oceanogr.*, 36, pp. 1471-1484.
- [5] Mori, N., Onorato, M., Janssen, P.A.E.M. et al., 2007. "On the extreme statistics of long-crested deep water waves: Theory and experiments", *J. Geophys. Res.*, 112, C09011(pp. 1-10).
- [6] Onorato, M., Osborne, A.R. and Serio, M., 2002. "Extreme wave events in directional, random oceanic sea states", *Phys. Fluids*, 14(4), pp. 25-28.
- [7] Soquet-Juglard, H., Dysthe, K., Trulsen, K. et al., 2005. "Probability distributions of surface gravity waves during spectral changes", *J. Fluid Mech.*, 542, pp. 195-216.
- [8] Waseda, T., Kinoshita, T. and Tamura, H., 2009. "Evolution of a random directional wave and freak wave occurrence", *J. Phys. Oceanogr.*, 39, pp. 621-638.
- [9] Onorato, M., Waseda, T., Toffoli, A. et al., 2009. "Statistical properties of directional ocean waves: the role of the modulational instability in the formation of extreme events", *Phys. Rev. Lett.*, 102(11), 114502(pp. 1-4).
- [10] Fujimoto, W., 2013. "Simulation of freak wave geometry with 3G wave model and High-Order Spectral Method", BS thesis, the University of Tokyo. [in Japanese].
- [11] Waseda, T. 2014., "Observational study of horizontal velocity of extreme waves", In WIN 2014, *Book of Abstracts of the international conference on Wave Interaction*, pp. 68-70.

- [12] Waseda, T., Tamura, H. and Kinoshita, T., 2012. "Freakish sea index and sea states during ship accidents", *J. Mar. Sci. Technol.*, 17(3), pp. 305-314.
- [13] Chaplin, J.R., 1996. "On frequency-focusing unidirectional waves", *Intl. J. Offshore Polar Eng.*, 6(2), pp. 131-137.
- [14] Tomita, H., Sawada, H., Ohmatsu, S. et al., 1997. "Study on dynamical and stochastic properties of breaking ocean waves", *Rep. Ship Res. Inst.*, 34(6), pp. 313-334. (in Japanese)
- [15] Clauss, G.F. and Kuhnlein, W.L., 1997. "Simulation of design storm wave conditions with tailored wave groups", *Proc. 7th Int. Offshore Polar Eng. Conf.*, 3, pp. 228-237.
- [16] Clauss, G.F., Hennig, J., Schmittner, C.E. et al., "Non-linear calculation of tailored wave trains for experimental investigations of extreme structure behavior", In OMAE 2004 – 23rd International Conference on Offshore Mechanics and Arctic Engineering. OMAE2004-51195.
- [17] Ueno, M., Miyazaki, H., Taguchi, H. et al., 2012, "Model experiment reproducing an incident of fast ferry", *J. Mar. Sci. Technol.*, 18(2), pp. 192-202.
- [18] Schmittner, C. and Hennig, J., 2012. "Optimization of short-crested deterministic wave sequences via a phase-amplitude iteration scheme", In OMAE 2012 – 31st International Conference on Ocean, Offshore and Arctic Engineering. OMAE2012-83150.
- [19] Zakharov, V. E., 1968. "Stability of periodic waves of finite amplitude on the surface of a deep fluid", *J. Appl. Mech. Tech. Phys.*, 9, pp. 190-204.
- [20] Benjamin, T.B., 1967. "Instability of periodic wavetrains in nonlinear dispersive systems", *Proc. R. Soc. Lond. A*, 299, pp. 59-76.
- [21] Tulin, M.P. and Waseda, T., 1999, "Laboratory observations of wave group evolution, including breaking effects", *J. Fluid Mech.*, 378, pp. 197-232.
- [22] West, B. J., Bruckner, K. A., Janda, R. S. et al., 1987. "A method of studying nonlinear random field of surface gravity waves by direct numerical simulation", *J. Geophys. Res.*, 92, pp. 803-824.
- [23] Dommermuth, D.G. and Yue, D.K.P., 1987, "A high-order spectral method for the study of nonlinear gravity waves", *J. Fluid Mech.*, 184, pp. 267-288.
- [24] Goullet, A. and Choi, W., 2011. "A numerical and experimental study on the nonlinear evolution of long-crested irregular waves", *Phys. Fluids*, 23, 016601(pp. 1-15).
- [25] Ducrozet, G., Bonnefoy, F., Touze, D.L. et al., 2012. "A modified High-Order Spectral method for wavemaker modeling in a numerical wave tank", *Eur. J. Mech. B/Fluids*, 34, pp. 19-34.
- [26] Tanizawa, K., Ueno, M., Taguchi, H. et al., 2011. "The Actual Sea Model Basin", *Rep. National Maritime Res. Inst.*, 10(4), 343-382. (in Japanese)
- [27] Havelock, T.H., 1929, "Forced surface waves on water", *Phil. Mag. Series 7*, 8(51), pp. 569-576.
- [28] Ursell, F., Dean, R.G. and Yu, Y.S., 1960. "Forced small-amplitude water waves : a comparison of theory and experiment", *J. Fluid Mech.*, 7, pp. 33-52.
- [29] Biesel, F. and Suquet, F., 1951. "Les appareils generateurs de houle en laboratoire", *La Huille Blanche*, 6(2,4,5). (in French). [English translation: Pilch, M. 1953. "Laboratory wave-generating apparatus", *St. Anthony Falls Hydraulic Laboratory Project Report*, 39].
- [30] Tasai, F., 1959. "On the damping force and added mass of ship heaving and pitching", *Rep. of Res. Inst. for Appl. Mech.*, 7(26), pp. 131-152.
- [31] Tasai, F., 1960. "Measurement of the wave height produced by the forced heaving of the cylinders", *Rep. of Res. Inst. for Appl. Mech.*, 8(29), pp. 279-310.
- [32] Flick, R.E. and Guza, R.T., 1980. "Paddle generated waves in laboratory channels", *J. WatWays., Port, Coastal and Ocean Div.*, 106(WW1), pp. 79-97.
- [33] Barthel, V., Mansard, E.P.D., Sand, S.E. et al., 1983. "Group bounded long waves in physical models", *Ocean Engng.*, 10(4), pp. 261-294.
- [34] Schaffer, H.A., 1996. "Second-order wavemaker theory for irregular waves", *Ocean Engng.*, 23(1), pp. 47-88.
- [35] Stokes, G.G., 1847. "On the theory of oscillatory waves", *Trans. Camb. Philos. Soc.*, 8, pp. 441-450.
- [36] Dommermuth, D., 2000. "The initialization of nonlinear waves using an adjustment scheme", *Wave Motion*, 32(4), pp. 307-317.
- [37] Frigaard, P., Hogedal, M., and Christensen, M., 1993. "Wave generation theory", *Hydraulics & Coastal Engineering Laboratory, Department of Civil Engineering, Aalborg University.*
- [38] Biesel, F., 1954. "Wave machines", *Proc. 1st Conf. on Ships and Waves*, Chapter 21, pp. 288-304.
- [39] Slunyaev, A.V. and Sergeeva, A.V., 2012. "Numerical simulations and analysis of spatio-temporal fields of rogue waves", *Fundament. Appl. Hydrophys.*, 5, pp. 24-36. (in Russian)
- [40] Gibson, R.S. and Swan, C., 2007. "The evolution of large ocean waves : the role of local and rapid spectral changes", *Proc. R. Soc. A.*, 463, pp. 21-48.
- [41] Krogstad, H.E. and Trulsen, K., 2010. "Interpretations and observations of ocean wave spectra", *Ocean Dyn.*, 60(4), pp. 973-991.
- [42] Tanizawa, K., 1996. "Long time fully nonlinear simulation of floating body motions with artificial damping zone", *J. Soc. Nav. Arch. Japan*, 180, pp. 311-319.
- [43] Tanaka, M., 2001. "A method of studying nonlinear random field of surface gravity waves by direct numerical simulation", *Fluid Dyn. Res.*, 28, pp. 41-60.
- [44] Tian, Z., Perlin, M. and Choi, W., 2008. "Evaluation of a deep-water wave breaking criterion", *Phys. Fluids*, 20, 066604 (pp. 1-13).
- [45] Waseda, T., Sinchi, M., Nishida, T. et al., 2011. "GPS-based wave observation using a moored oceanographic buoy in the deep ocean", *Proc. 21st Int. Offshore Polar Eng. Conf.*, pp. 365-372.

- [46] Waseda, T., Sinchi, M., Kiyomatsu, K. et al., 2014. "Deep water observations of extreme wave with moored and free GPS buoy", *Ocean Dyn.*, *64*, pp. 1269-1280.
- [47] Kuik, A.J., Van Vledder, G.Ph. and Holthuijsen, L.H., 1988. "A method for the routine analysis of pitch-and-roll buoy wave data", *J. Phys. Oceanogr.*, *18*, pp. 1020-1034.